Chemical Physics Letters 545 (2012) 83–87

Contents lists available at SciVerse ScienceDirect

Chemical Physics Letters

journal homepage: www.elsevier.com/locate/cplett

Binding properties of a nitrogen atom onto an anionic golden fullerene Au_{16}^-

Gunn Kim [a,*], Seoung-Hun Kang [b], Chan-young Lim [d], Young-Kyun Kwon [c,*]

[a] Department of Physics, Graphene Research Institute and Institute of Fundamental Physics, Sejong University, Seoul 143-747, Republic of Korea
[b] Department of Physics and Research Institute for Basic Sciences, Kyung Hee University, Seoul 130-701, Republic of Korea
[c] Department of Physics, Research Institute for Basic Sciences, and Research Center for New Nano Bio Fusion Technology, Kyung Hee University, Seoul 130-701, Republic of Korea
[d] Sejong Science High School, Seoul 152-881, Republic of Korea

ARTICLE INFO

Article history:
Received 30 January 2012
In final form 11 July 2012
Available online 20 July 2012

ABSTRACT

Using density functional theory, we examine the effects of a nitrogen atom adsorbed onto an anionic golden cage (Au_{16}^-) on the properties of the nanocage. For the exohedral adsorption that is more stable than the endohedral doping, the bridge and hollow sites have larger binding energies than the atop sites by ~1 eV. When the N atom is adsorbed on the cage, electrons are transferred to nitrogen from Au_{16}^-. The nitrogen atom may move thermally from the exterior to the interior through a bridge site. In infrared spectra, exohedral doping causes greater intensities at higher frequencies than endohedral doping.

1. Introduction

Since their discovery, carbon fullerene molecules such as C_{60}, C_{70}, and C_{80} have caught considerable attention because of their attractive electronic, optical, and electrochemical properties [1–4]. Interestingly, it was proved experimentally that carbon fullerenes have cousins made of metal, in particular, golden fullerenes. In 2006, Bulusu and colleagues showed experimental and theoretical evidence of anionic hollow golden cages, Au_n^- ($n = 16 - 18$) [5]. They compared experimental photoelectron spectra of the anionic structures with those simulated by density functional theory (DFT) [6].

Au_{16}^- is the smallest golden cage with an empty interior. It has slightly distorted tetrahedral symmetry (T_d), with an inner diameter of ≈5.5 Å. Thus, it is possible to endohedrally dope the golden cage in analogy to the carbon fullerenes. Numerous theoretical and experimental studies of metal atoms adsorbed on the golden cages have been reported [7–10]. Similar to carbon fullerene derivatives, the golden fullerene can become a host to form various derivatives by adsorbing various atoms, molecules and radicals. Recently, due to their high reactivity, gold nanoclusters have been explored for their potential use for nanocatalysts [11–14].

In this Letter, we report our study on a golden cage anion, Au_{16}^-, doped with a nitrogen atom which is a non-metal atom [15]. Since oxidation is an important issue for gold nanostructures with high chemical reactivity, we have investigated the binding characteristics of the adsorbate atom on Au_{16}^-. Nitrogen is an element with a large electron affinity, and so the adsorbed N atom may accept electrons from the golden fullerene. Going a step further, it may help to understand adsorption properties of molecules containing nitrogen such as N_2, NO, NO_2, and NH_3, onto the golden buckyball. We also investigate the transition between the most favorable exohedral and endohedral adsorption configurations. Finally, we show the infrared (IR) active vibrational spectra of our models, which may help identify N-adsorbed Au_{16}^- in future experiments.

2. Computational methods and model structures

To study the binding properties of a nitrogen atom on Au_{16}^-, we performed first-principles calculations within DFT with spin polarization implemented in the DMOL^3 package [16]. We used the generalized gradient approximation with the Perdew–Burke–Ernzerhof functional [17] to describe the exchange–correlation. To expand the electronic wavefunctions, a double-numerical polarized basis set was chosen with a real space cutoff of 6.5 Å. The scalar relativistic effects were included in the all-electron calculation. For more precise computations, we chose an octupole scheme for the multipolar fitting procedure on the charge density and a fine grid scheme for numerical integration [18].

The cluster geometry was optimized by the Broyden–Fletcher–Goldfarb–Shanno algorithm [19–23] without symmetry constraints until the total energy change was converged to 10^{-5} Ha in the self-consistent loop and the atomic forces were smaller than 4×10^{-4} Ha Å^{-1}. The optimized geometries of NAu_{16}^- were determined from the total energy minimum, and were further verified by the absence of imaginary frequencies in the harmonic frequency calculations. Using the nudged elastic band (NEB) method [24], we searched for the minimum-energy path in geometrical phase space connecting two stable structures. Including the initial and final

* Corresponding authors.
E-mail addresses: gunnkim@sejong.ac.kr (G. Kim), ykkwon@khu.ac.kr (Y.-K. Kwon).

0009-2614/$ - see front matter © 2012 Elsevier B.V. All rights reserved.
http://dx.doi.org/10.1016/j.cplett.2012.07.025

configurations, 20 replicas were chosen to construct the NEB. For a trajectory of the minimum-energy path between reactants and products during the atomic encapsulation, linear synchronous transit and quadratic synchronous transit (LST/QST) calculations [25,26] were also performed with conjugate gradient minimization [27]. Finally, IR-active vibrational spectra were evaluated for our models by calculating the dynamical matrix [28] and the Born effective charge tensor [29].

As in our previous study [15], we considered various endohedral and exohedral adsorption sites for the initial configurations, as clearly shown in Figure 1. Au_{16}^- looks like a truncated tetrahedron. The truncated tetrahedron is created by cutting off the tips of the tetrahedron one third of the way into each edge. It has 4 equilateral triangles and 4 regular hexagons. Au_{16}^- is also composed of 4 hexagonal facets and 4 triangular facets (TR1) formed by the truncation [15]. In particular, each hexagonal facet in Au_{16}^- consists of 6 triangles. As depicted in Figure 1, they are geometrically different from TR1 (the truncated triangle), and are classified into two types, TR2 and TR3. TR2 shares an edge with an adjacent TR1 and two edges with two TR3 triangles in the same hexagonal facet, whereas TR3 has a common junction with another TR3 located on a neighboring hexagonal facet, and two junctions with two TR2 triangles in the same hexagonal facet. Three TR2 and three TR3 triangles are arranged alternately on each hexagonal facet. Two types of vertices or atop sites are also considered: AT1 and AT2. AT1 represents 12 equivalent vertices forming four TR1 triangles, and the remaining four vertices located at the center of each hexagonal facet fall into the other type, AT2. In addition, edges shared by two neighboring triangles or bridges between two Au atoms can be classified into three types, BR1, BR2, and BR3. Figure 1 shows that BR1 is shared by TR1 and TR2; BR2 is done by TR2 and TR3 in the same hexagonal facet; and BR3 by two TR3 triangles, one in a hexagonal facet and the other in a neighboring hexagonal facet. Overall, there exist eight different adsorption sites on the outer surface of Au_{16}^-, as shown in Figure 1.

We also considered the encapsulation inside Au_{16}^- as 'adsorption' sites for endohedral doping of the N atom [15]. Together with the center (CTR) of the Au_{16}^- cluster, eight more off-centered encapsulation configurations labeled "In-XX*n*" corresponding to the eight exohedral sites (XX*n*, XX = TR, BR, or AT, and $n = 1$, 2, or 3). Our DFT calculations demonstrate that only CTR and In-BR3 sites are stable among all endohedral doping sites, and the other seven adsorption configurations tend to change into either In-BR3 or CTR during structural relaxation.

3. Results and discussion

For each configuration shown in Figure 1, we obtained the equilibrium geometry of NAu_{16}^- and its binding energy (E_b) defined by

$$E_b = E[Au_{16}^-] + E[N] - E[NAu_{16}^-],$$

where $E[NAu_{16}^-]$ and $E[Au_{16}^-]$ are the total energies of the golden cage with and without a nitrogen atom, respectively, and $E[N]$ represents the energy of an isolated N atom. All the calculated energy values are summarized in Table 1. Here, a positive (negative) sign in E_b means an exothermic (endothermic) process. We found that two triangular sites (TR1 and TR2) and one bridge site (BR3) are favored by the N atom. TR1 is the most preferred adsorption site with the binding energy of 2.95 eV, and BR3 (TR2) has the binding energy of 2.90 eV (2.80 eV). The binding energy for the TR3 site is not as large as those for TR1 and TR2, as listed in Table 1. By contrast, the atop sites (AT1 and AT2) are less preferable (≈1.7 eV at AT1 and ≈1.1 eV at AT2). The N atom that was initially located at BR1 spontaneously moved to TR2 during structural relaxation, implying that BR1 is an unstable adsorption site.

We also calculated the encapsulation energy, which is regarded as an energy gain due to endohedral doping. For the CTR site, the encapsulation energy for the nitrogen atom is 0.58 eV, which is much smaller than the binding energies on all the exohedral adsorption sites. Intriguingly, the only stable off-centered adsorption site, In-BR3, shows much bigger encapsulation energy (1.95 eV) than CTR. As shown in Figure 1, in the In-BR3 case, the endohedrally-doped N atom appears to elongate the Au-Au bond corresponding to BR3 and draws two Au atoms (corresponding to AT2), compared to its exohedral counterpart, BR3.

Using the charge density difference, we investigated the charge redistribution induced by the N atom adsorption. Figure 2a–c display the charge density differences of TR1, the most stable exohedral adsorption site, and CTR and In-BR3, two stable endohedral adsorption sites. The charge differences reveal dumbbell-like shapes with two lobes at the positions of adjacent gold atoms. The charge transfer (ΔQ) between the adsorbate and the golden fullerene was also calculated using the Mulliken population analysis. As listed in Table 1, electrons are donated from Au_{16}^- to the N atom for all the configurations. CTR shows the smallest amount of charge transfer, whereas In-BR3 does the largest charge transfer. We also analyzed the local magnetic moments of our model systems. It was found that among the adsorption configurations we considered, only CTR has the spin magnetic moment of ≈2.1 μ_B, where

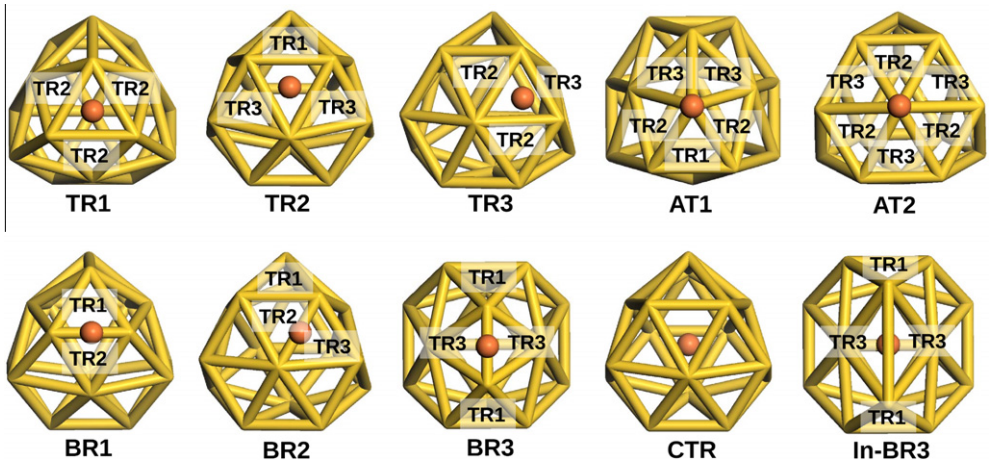

Figure 1. Atomic model structures of the nitrogen atom adsorbed on Au_{16}^-. Ten adsorption sites of the adsorbate are considered: three different triangular sites, TR1, TR2, and TR3; three dissimilar bridge sites, BR1, BR2, and BR3; two inequivalent atop sites, AT1 and AT2; and two selected endohedral doping sites, CTR and In-BR3. For the detailed classification of these adsorption sites, see the text.

Table 1
The binding energy (E_b), the HOMO–LUMO gap (E_{gap}), the distance between the nitrogen atom and its nearest gold atoms in the golden cage (d_{Au-N}), and the amount of electronic charge transferred from Au_{16}^- to the adsorbate atom (ΔQ) at the different adsorption sites shown in Figure 1.

Configuration	N on Au_{16}^-			
	E_b (eV)	E_{gap} (eV)	d_{Au-N} (Å)	ΔQ (e)
TR1	2.95	0.14	1.98	−0.513
TR2	2.80	0.83	2.03	−0.477
TR3	1.73	0.13	2.36	−0.486
BR2	2.57	0.32	1.94	−0.404
BR3	2.90	0.64	1.91	−0.439
AT1	1.68	0.57	1.84	−0.353
AT2	1.12	0.68	1.87	−0.323
CTR	0.58	0.69	2.20	−0.142
In-BR3	1.95	0.26	2.05	−0.630

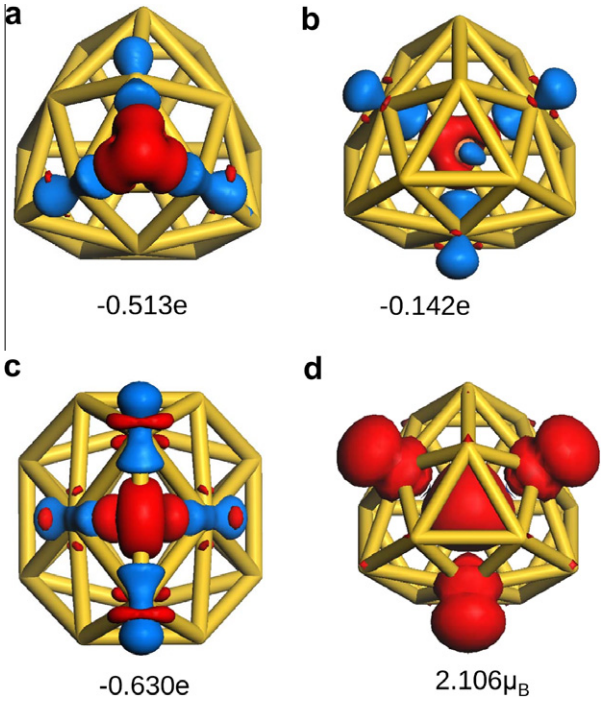

Figure 2. The isosurface plots of the charge density difference for (a) TR1, (b) CTR and (c) In-BR3. The electron accumulation is represented in red, and the depletion in blue. The negative value shown at the bottom of each structure represents the amount of electrons transferred from the golden cage to the N atom. (d) The spin density plot of the CTR structure. Its net magnetic moment is calculated to be 2.106 μ_B, where μ_B is the Bohr magneton. The isovalue is ±0.005 e Å^{-3}. (For interpretation of the references to color in this figure legend, the reader is referred to the web version of this article.)

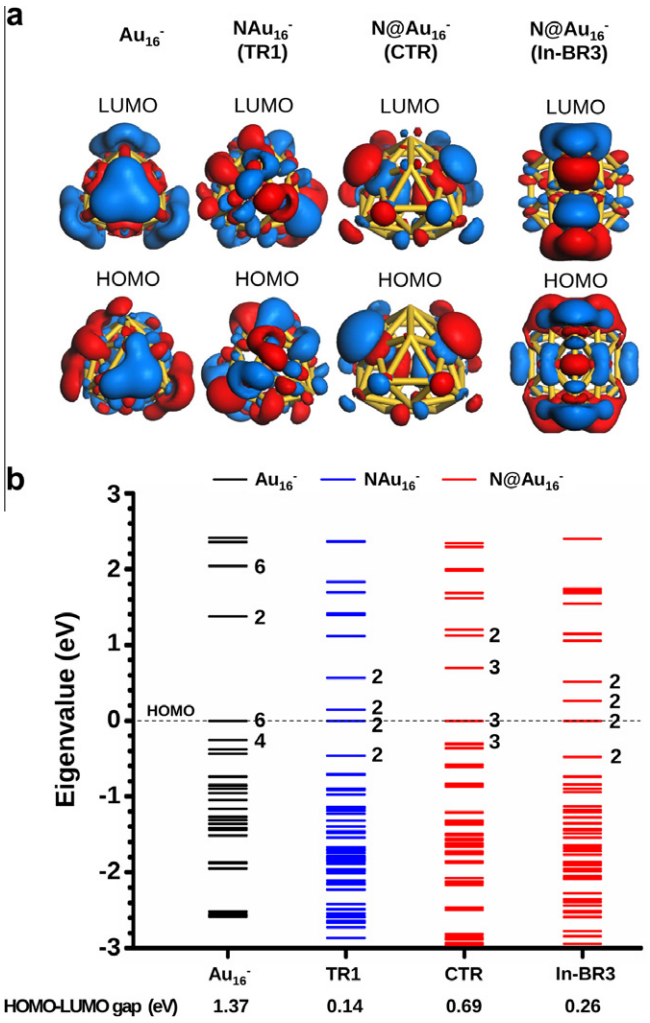

Figure 3. (a) The HOMOs and LUMOs of the bare Au_{16}^- cage, the most stable exohedrally adsorbed structure (TR1) of NAu_{16}^-, and the N-encapsulated structures (CTR and In-BR3) of $N@Au_{16}^-$. The isovalue is ±0.02 e Å^{-3}. (b) Energy levels near the HOMOs and the LUMOs of the four structures given in (a). The numbers written next to the energy levels represent the degeneracy of respective levels. The HOMO level of every structure is set to zero. For each configuration, the HOMO–LUMO energy gap is given at the bottom of the graph.

μ_B is the Bohr magneton ($\approx 5.788 \times 10^{-5}$ eV T^{-1}, where T denotes the tesla, the unit of magnetic flux density). Figure 2d shows the spin density plot of CTR, where the majority spin density is distributed only at the Au atoms corresponding to AT2 as well as at the N atom at the center. The minority spin density does not appear for the isovalue of ±0.005 e Å^{-3}.

Next we analyzed the energy eigenvalues and the corresponding molecular orbitals (eigenfunctions) of our various configuraions of the N-adsorbed golden cage. Figure 3a displays the highest occupied molecular orbitals (HOMOs) and lowest unoccupied molecular orbitals (LUMOs) of the three configurations of the N-adsorbed cage shown in Figure 2a–c, as well as of the bare golden cage for comparison. Obviously, antibonding molecular orbitals are found between the N and Au atoms. The adsorption of the nitrogen atom causes the breaking of the tetrahedral symmetry, resulting in level splitting, as shown in Figure 3b. The HOMO–LUMO energy gaps are 0.14, 0.69, and 0.26 eV for TR1, CTR, and In-BR3, respectively. All of them are much smaller than that (1.37 eV) of bare Au_{16}^-.

To evaluate the activation energy barrier associated with nitrogen atom encapsulation, which plays a pivotal role in the reaction rate of the dopant insertion, we obtained the minimum-energy path in the configuration space using the NEB method. Figure 4a is an illustration of the energy profile in the transformation between the stable exohedral and endohedral adsorption configurations, showing the activation barrier (E_a), and reaction energy (E_r) defined by the energy difference between the reactant and the product. Because any triangular site can be a gate for atomic insertion, we first considered three paths: TR1 → CTR, TR2 → CTR, and TR3 → CTR. In these cases, three Au–Au bonds are maximally stretched in the transition states during insertion of the dopant atom. We found that the activation energy barriers along all the three paths are almost the same (≈2.7 eV). These similar activation barriers are strongly related to the maximally elongated Au–Au bond lengths, which are essentially the same in all three cases, as displayed in the middle column of Figure 4b representing the

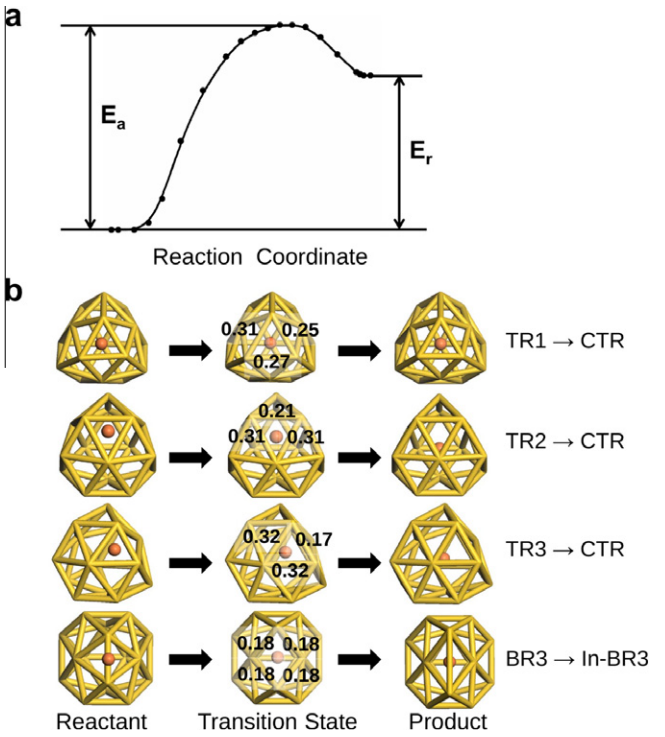

Figure 4. (a) Schematic energy profile along the reaction coordinates. The dots represent the energies of the replicas in the transformation for the NEB method. The activation energy barrier E_a and the reaction energy E_r are defined by the encapsulation barrier from the reactant and the energy difference between the reactant and the product, respectively. (b) Atomistic model structures for various reaction paths from reactants to products. The first three figures display the transitions of the N atom from three triangular sites (TR1, TR2, and TR3) to the CTR site, whereas the last one depicts that from BR3 to In-BR3, the off-centered site. The values marked in the middle represent the maximal elongations Δd_{Au-Au} in Åfrom the equilibrium distances between two neighboring Au atoms located near the N atom during the encapsulation process.

transition states. On the other hand, the reaction energy of the TR3 → CTR path is about 1.2 eV smaller than the other two paths, since TR3 has a smaller binding energy with a longer Au–N distance than TR1 and TR2 (see Table 1).

We also checked the BR3 → In-BR3 path, since BR3 and In-BR3 are also stable exohedral and endohedral configurations. Interestingly, for the BR3 → In-BR3 path, a single Au–Au bond corresponding to BR3 is broken to form Au–N–Au and at the same time the N atom tend to draw two Au atoms located at two nearest AT2 sites. In this transition, the activation energy barrier is much smaller (1.51 eV) than those of three paths through the triangular sites. In addition, much more stable In-BR3 configuration than CTR for the N encapsulation shows much lower reaction energy (0.94 eV). Consequently, we conclude that the transition path occurring through a single Au–Au bond stretch may be preferred in the N atom encapsulation process. The calculated activation barriers (E_a) and reaction energies (E_r) are summarized in Table 2.

The encapsulation events through any triangular site would not take place even near the melting temperature of the golden fullerene, while the insertion event though the BR3 site may occur at relatively low temperature without any external aids. According to our estimation, the probabilities that such transitions happen are $\sim 10^{-11}$ s^{-1} for TR1 → CTR, and $\sim 10^{-3}$ s^{-1} for BR3 → In-BR3 at 600 K. The insertion events would be even enhanced with the help of light or electron-beam irradiation, as shown in earlier experiments. It was shown that electron-beam irradiation has been used to fuse C_{60} fullerenes inside host carbon nanotubes [30] and the scanning tunneling microscope has induced a cis–trans conformation change in the azobenzene molecule [31].

Table 2
The activation energy barriers (E_a) and the reaction energies (E_r) for the four transitions described in Figure 4

	System	E_a (eV)	E_r (eV)
NAu_{16}^-	TR1 → CTR	2.71	2.37
	TR2 → CTR	2.71	2.22
	TR3 → CTR	2.74	1.15
	BR3 → In-BR3	1.51	0.94

Finally, we calculated the IR active vibrational spectra of two most stable exohedral doping configurations (TR1 and BR3), and an endohedral configuration (CTR). We believe that the IR spectroscopy could be used to distinguish structures with different adsorption sites. Figure 5 shows our computationally simulated IR intensity data for the three configurations. For comparison, we also calculated the IR spectrum for the bare Au_{16}^- cage, displayed

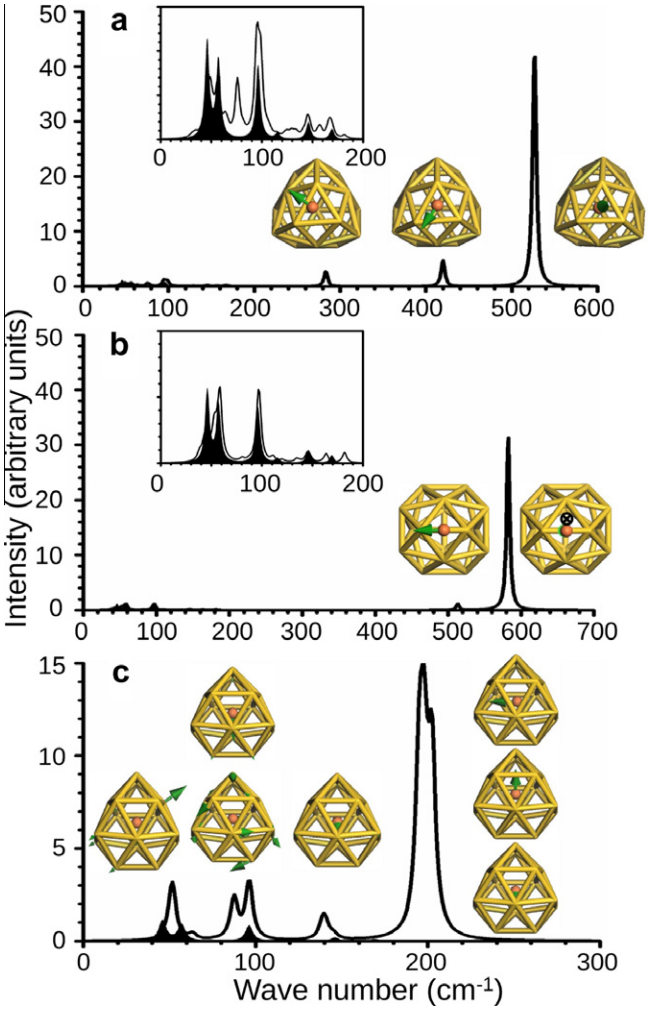

Figure 5. The IR-active modes for (a) the most stable exohedral adsorption structure (TR1), (b) the next most stable exohedral adsorption structure (BR3), and (c) an endohedrally doped $N@Au_{16}^-$ (CTR). The IR-active modes for the bare Au_{16}^- cage are displayed in solid black in each figure. Detailed IR spectra at wavenumbers below 200 cm^{-1} are shown in the insets for the exohedral cases. The model structures with green arrows are shown at the peaks to denote the directions and the intensities of the IR-active modes contained in each peak. In (b), the symbol ⊗ indicates that the nitrogen atom moves towards the center of the Au–Au bond. (For interpretation of the references to color in this figure legend, the reader is referred to the web version of this article.)

in solid black in each figure. Its strong IR intensities are observed in the frequency range below 200 cm^{-1}, since Au is one of heavy elements, whose frequency is inversely proportional to $\sqrt{m}$, where m is the atomic mass. We found that three modes with dominant intensities arise at the frequencies of 45, 56, and 96 cm^{-1} corresponding to an Au–Au bond stretching mode and several weak modes. In the case of the TR1 configuration, the strongest peak appears at much higher frequency of ≈520 cm^{-1} as well as two weak peaks at ≈280 and ≈420 cm^{-1} due to the N adsorbate, as shown in Figure 5a. For the BR3 configuration, the strongest peak arises at even higher frequency of ≈580 cm^{-1} with a very weak peak near ≈520 cm^{-1}. It means that BR3 is spectroscopically distinguishable from TR1. The direction and the relative intensity of each peak are denoted by the green arrows.

On the other hand, the insertion of the N atom at the center combines two lowest modes (45 and 56 cm^{-1}) of the bare golden cage into one mode while keeping the mode around 96 cm^{-1}, as displayed in Figure 5c. Three other peaks are observed near 90, 140 and 200 cm^{-1}. As denoted by the green arrows in Figure 5c, all of them are due to the vibration motion of the N atom encapsulated at the center of the golden fullerene. Especially, the broad peak at 200 cm^{-1} is composed of three IR-active modes. These highest IR-active modes occur at much lower frequencies, compared with TR1 and BR3. This is attributed to the almost flat potential surface of the N atom around the center of Au_{16}^- resulting in a small force constant.

4. Conclusion

In summary, we studied the binding effects of a nitrogen atom on the structural and electronic properties of an anionic golden fullerene Au_{16}^- using density functional theory. The general trend is that the triangular (hollow) and bridge sites are preferred for exohedral nitrogen adsorption. When the N atom is adsorbed on the cage, electrons are transferred from Au_{16}^- to the N atom. We also searched for the minimum-energy transition paths between the stable exohedral and endohedral adsorption configurations, and obtained the activation energy and reaction energy for each path. It was found that the transitions from the triangular sites to the center of Au_{16}^- would not take place with an activation energy of about 2.7 eV and a reaction energy of 1.2–2.4 eV implying no such transition without an external aid. On the other hand, we found that the transition through an Au–Au bond may take place even at ambient temperatures, since the transition energy barrier is much lower. The IR spectra for various adsorption configurations were also computed. In the exohedral doping cases, the dominant IR peaks occur at higher frequencies with larger intensities than in the endohedral doping cases. Our study may help design new types of small gold nanocluster derivatives. On the basis of our present Letter, further studies will be carried out on the binding properties of nitrogen-containing molecules such as N_2, NO, NO_2 and NH_3 on the golden cage.

Acknowledgments

G.K. thanks the Basic Research Program (Grant No. 2012-0001743) and the Priority Research Center Program (Grant No. 2012-0005859) of the Korean Government Ministry of Education, Science and Technology. Y.K. gratefully acknowledges the financial support from the National Research Foundation of Korea (Grant Nos. 2011-0002456 and 2011-0016188). Some portion of our computational work was done using the resources of the KISTI Supercomputing Center (KSC-2011-C1-04 and KSC-2011-C1-19).

References

[1] S.H. Friedman, D.L. DeCamp, R.P. Sijbesma, G. Srdanov, F. Wudl, G.L. Kenyon, J. Am. Chem. Soc. 115 (1993) 6506.
[2] M. Prato, M. Maggini, Acc. Chem. Res. 31 (1998) 519.
[3] L. Echegoyen, L.E. Echegoyen, Acc. Chem. Res. 31 (1998) 593.
[4] D.M. Guldi, M. Prato, Acc. Chem. Res. 33 (2000) 695.
[5] S. Bulusu, X. Li, L.S. Wang, X.C. Zheng, Proc. Natl. Acad. Sci. USA 103 (2006) 8326.
[6] P. Hohenberg, W. Kohn, Phys. Rev. 136 (1964) B864.
[7] M. Walter, H. Hakkinen, Phys. Chem. Chem. Phys 8 (2006) 5407.
[8] Q. Sun, Q. Wang, G. Chen, P. Jena, J. Chem. Phys. 127 (2007) 214706.
[9] L.M. Wang, S. Bulusu, H.J. Zhai, X.C. Zeng, L.S. Wang, Angew. Chem. Int. Ed. 46 (2007) 2915.
[10] W. Fa, A. Yang, Phys. Lett. A 372 (2008) 6392.
[11] B. Yoon, H. Hkkinen, U. Landman, J. Phys. Chem. A 107 (2003) 4066.
[12] M. Valden, X. Lai, D.W. Goodman, Science 281 (1998) 1647.
[13] U. Heiz, W.D. Schneider, J. Phys. D: Appl. Phys. 33 (2000) R85.
[14] H.-G. Boyen et al., Science 297 (2002) 1533.
[15] S.-H. Kang, G. Kim, Y.-K. Kwon, J. Phys.: Condens. Matter 23 (2011) 505301.
[16] B. Delley, J. Chem. Phys. 92 (1990) 508.
[17] J.P. Perdew, K. Burke, M. Ernzerhof, Phys. Rev. Lett. 77 (1996) 3865.
[18] E.J. Baerends, D.E. Ellis, P. Ros, Chem. Phys. 2 (1973) 41.
[19] C.G. Broyden, J. Instr. Math. Appl. 6 (1970) 76.
[20] R. Fletcher, Comput. J. 13 (1970) 317.
[21] D. Goldfarb, Math. Comput. 24 (1970) 23.
[22] D.F. Shanno, Math. Comput. 24 (1970) 647.
[23] D.F. Shanno, P.C. Kettler, Math. Comput. 24 (1970) 657.
[24] G. Henkelman, H. Jonsson, J. Chem. Phys. 113 (2000) 9978.
[25] J. Baker, J. Comput. Chem. 7 (1986) 385.
[26] C.J. Cerjan, W.H. Miller, J. Chem. Phys. 75 (1981) 2800.
[27] N. Govind, M. Petersen, G. Fitzgerald, D. King-Smith, J. Andzelm, Comput. Mater. Sci. 28 (2003) 250.
[28] E.B. Wilsun, J.C. Decius, P.C. Cross, Molecular Vibrations, Dover, New York, 1980.
[29] S. Baroni, S. de Gironcoli, A. dal Corso, P. Giannozzi, Rev. Mod. Phys. 73 (2001) 515.
[30] S. Bando, M. Takizawa, K. Hirahara, M. Yudasaka, S. Iijima, Chem. Phys. Lett. 337 (2001) 48.
[31] B. Choi et al., Phys. Rev. Lett. 96 (2006) 156106.